

Role of clustered nuclear geometry in particle production through p–C and p–O collisions at the Large Hadron Collider

Aswathy Menon K R,^{*} Suraj Prasad,[†] Neelkamal Mallick,[‡] and Raghunath Sahoo[§]
Department of Physics, Indian Institute of Technology Indore, Simrol, Indore 453552, India
 (Dated: July 8, 2024)

Long-range multi-particle correlations in heavy-ion collisions have shown conclusive evidence of the hydrodynamic behavior of strongly interacting matter, and are associated with the final-state azimuthal momentum anisotropy. In small collision systems, azimuthal anisotropy can be influenced by the hadronization mechanism and residual jet-like correlations. Thus, one of the motives of the planned p–O and O–O collisions at the LHC and RHIC is to understand the origin of small system collectivity. As the anisotropic flow coefficients (v_n) are sensitive to the initial-state effects including nuclear shape, deformation, and charge density profiles, studies involving ^{12}C and ^{16}O nuclei are transpiring due to the presence of exotic α (^4He) clusters in such nuclei. In this study, for the first time, we investigate the effects of nuclear α -clusters on the azimuthal anisotropy of the final-state hadrons in p–C and p–O collisions at $\sqrt{s_{\text{NN}}} = 9.9$ TeV within a multi-phase transport model framework. We report the transverse momentum (p_{T}) and pseudorapidity (η) spectra, participant eccentricity (ϵ_2) and triangularity (ϵ_3), and estimate the elliptic flow (v_2) and triangular flow (v_3) of the final-state hadrons using the two-particle cumulant method. These results are compared with a model-independent Sum of Gaussians (SOG) type nuclear density profile for ^{12}C and ^{16}O nuclei.

I. INTRODUCTION

The world’s most powerful particle accelerators, the Relativistic Heavy-Ion Collider (RHIC) at BNL, USA, and the Large Hadron Collider (LHC) at CERN, Switzerland, offer unparalleled experimental capabilities to perform high-energy hadronic and nuclear collisions to study the behavior of nuclear matter under extreme conditions of temperature and baryon density. Such ultra-relativistic heavy-ion collisions produce a state of locally thermalized and deconfined partonic medium, known as the quark-gluon plasma (QGP). While the existence of QGP has long been established in heavy-ion collisions, its presence in small collision systems is a matter of intense research, recently. Thanks to the recent measurements of heavy-ion-like features in high multiplicity pp collisions such as strangeness enhancement [1], ridge-like structure [2, 3], and radial flow effects [4–6], the possible existence of QGP droplets in small collision systems needs to be re-examined. As p–C and p–O collisions fill the multiplicity gap between pp to p–Pb and peripheral Pb–Pb collisions, it provides a perfect system size for studying several heavy-ion-like effects in small collision systems at the RHIC and LHC energies [7, 8].

In non-central heavy-ion collisions, the appearance of strong final-state azimuthal momentum anisotropy is associated with the hydrodynamic collective expansion of the medium [9, 10]. This collectivity is usually quantified as the Fourier coefficients (v_n) of the final-state azimuthal momentum distribution ($dN/d\phi$) [11, 12]. Azimuthal

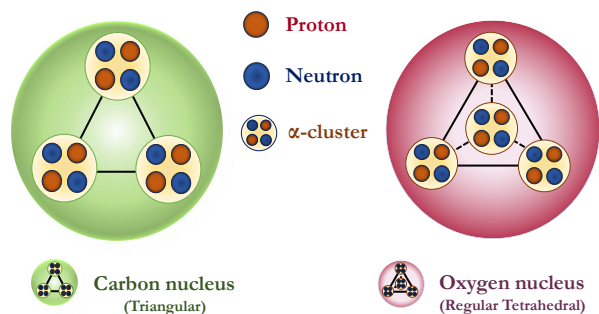


FIG. 1. (Color online) Pictorial representation of the arrangement of α -particles inside ^{12}C (left) and ^{16}O (right) nucleus.

anisotropy mainly arises from the initial nuclear geometry and fluctuations in the energy and entropy density, which further gets embedded in the system through its equation-of-state and transport coefficients [9, 10]. Hydrodynamic model predictions when confronted with the experimental findings have shown conclusive evidence of the collective expansion of the thermalized medium and strongly hint at the formation of QGP in heavy-ion collisions [13]. However, such collective behavior is usually not anticipated in small collision systems, thus, the applicability of hydrodynamics, and hence, thermalization in the early stages of the collision is still debatable in small collision systems.

The anisotropic flow coefficients, such as elliptic flow (v_2) and triangular flow (v_3), are found to be sensitive to the initial nuclear distribution, nuclear shape deformation, and fluctuations in the nuclear overlap region [14–16]. In Xe–Xe collisions at the LHC, the presence of a deformed nuclear structure gives rise to a higher value of elliptic flow in the most central collisions compared to

^{*} Aswathy.Menon@cern.ch

[†] Suraj.Prasad@cern.ch

[‡] Neelkamal.Mallick@cern.ch

[§] Corresponding author: Raghunath.Sahoo@cern.ch

Pb–Pb collisions [17–20]. In addition, a larger density fluctuation due to a smaller number of participating nucleons in Xe–Xe collisions gives rise to a larger value of triangular flow in contrast to Pb–Pb collisions [17, 18]. A similar study using AMPT in U–U collisions at the RHIC energy shows that the values of anisotropic flow coefficients change with a change in the deformation parameter of the nuclear distribution [14]. However, the impact of this deformation is larger for elliptic flow in contrast to the triangular flow [14, 15, 21]. In addition, recent observations of ridge-like structures in p–Pb collisions have brought significant attention to asymmetric collisions, which are customarily considered to provide a baseline measurement for the cold nuclear effects [6, 22–25], where the presence of strong long-range multi-particle correlations are not expected. Further, the measured values of anisotropic flow coefficients in p–Pb collisions are comparable to that of peripheral Pb–Pb collisions [26–28]. Although, in p–Pb collisions, the ordering of the magnitude of flow coefficients, i.e., $v_2 > v_3 > v_4$, is not as strong as in Pb–Pb collisions, the bare presence of signatures of collectivity in p–Pb collisions makes the study of asymmetric collisions a vital contribution of the heavy-ion physics community.

Nuclei having $4n$ number of nucleons, are theorized to have α -clusters (${}^4\text{He}$ -nucleus), which include ${}^8\text{Be}$, ${}^{12}\text{C}$, and ${}^{16}\text{O}$ nuclei. In ${}^{12}\text{C}$, the α -particles arrange themselves at the corners of an equilateral triangle. Similarly, nucleons inside ${}^{16}\text{O}$ are expected to configure themselves in four α -clusters forming a regular tetrahedral geometry [29–34]. Figure 1 shows the pictorial representation of the arrangement of nucleons inside an α -particle, and the arrangement of α -clusters inside ${}^{12}\text{C}$ (left) and ${}^{16}\text{O}$ (right) nuclei. Studies involving ${}^{12}\text{C}$ and ${}^{16}\text{O}$ nuclei have the potential to explore the emergence of collectivity in small systems in addition to the study of α -cluster nuclear geometry effects on the final-state observables. Additionally, studies involving forward kinematics in p–O collisions are crucial in understanding the interaction of cosmic rays (mostly protons) with the Earth’s atmosphere (mostly ${}^{14}\text{N}$ and ${}^{16}\text{O}$). It could also help resolve the outstanding muon puzzle and perform precise measurements of the π^0 energy fraction ($R = E_{\pi^0}/E_{\text{all hadrons}}$), a smaller value of which is potentially attributed to strangeness enhancement, and hence hints towards the formation of QGP droplets [7].

With all these tempting motivations, in recent years, several studies have been performed involving collisions of ${}^{12}\text{C}$ and ${}^{16}\text{O}$ nuclei [16, 35–41]. It includes the studies based on different hydrodynamic models [42–44], Glauber Monte Carlo [35–37], parton energy loss [45], and jet quenching effects [46]. Some of these studies also investigate the possible signatures of α -clusters in ${}^{12}\text{C}$ and ${}^{16}\text{O}$ nuclei by studying the final-state particle production and anisotropic flow measurements [16, 39–41, 47–51]. In Ref. [40], an enhanced value of triangular flow in C–Au collisions is observed for an α -clustered ${}^{12}\text{C}$ nucleus. In Ref. [16], authors show that the pres-

ence of an α -clustered structure in ${}^{16}\text{O}$ nucleus leads to a high value of triangular flow in most central O–O collisions, which are well observed in the ratio v_3/v_2 . In addition, an away-side broadening in the two-particle correlation function is also reported for O–O collisions with α -clusters as compared to the Woods-Saxon nuclear profile [16]. Although there have been a few studies that aim to establish a clear signature of the presence of α -clusters in ${}^{16}\text{O}$ and ${}^{12}\text{C}$ nucleus, the choice of p–O and p–C is novel to this study. In addition, the studies of anisotropic flow in asymmetric collision systems like p–O and p–C can accord the observations of collectivity in p–Pb collisions.

In this study, we incorporate an α -cluster-type initial geometry for ${}^{12}\text{C}$ and ${}^{16}\text{O}$ nuclei, and report the first measurements of transverse momentum (p_T) and pseudorapidity (η) spectra, participant eccentricity (ϵ_2) and triangularity (ϵ_3), and elliptic flow (v_2) and triangular flow (v_3) of the final-state hadrons, and their scaling in p–O and p–C collisions at $\sqrt{s_{\text{NN}}} = 9.9$ TeV using a multi-phase transport model (AMPT). We use the two-particle cumulant method with a relative pseudorapidity cut to minimize the effects of nonflow correlations. These results are compared with a model-independent Sum of Gaussians (SOG) type nuclear density profile for ${}^{12}\text{C}$ and ${}^{16}\text{O}$ nuclei.

The paper is organized as follows. We start with a brief introduction and motivation of the study in Section I followed by a description of event generation and methodology in Section II. In Section III, we present and discuss the results. Finally, in Section IV, we summarize the study with important findings and present a brief outlook for future research.

II. EVENT GENERATION AND METHODOLOGY

In this section, we begin with a brief introduction to a multi-phase transport model, which is used to simulate p–C and p–O collisions at $\sqrt{s_{\text{NN}}} = 9.9$ TeV. The technical details of the implementation of different nuclear profiles for ${}^{16}\text{O}$ and ${}^{12}\text{C}$ nuclei are discussed next. Finally, a detailed description of the two-particle cumulant method for the anisotropic flow estimation is provided.

A. A multi-phase transport model

AMPT is a widely used Monte Carlo transport model constructed to describe the space-time evolution of pp, p+A, and A+A collisions across RHIC and LHC energies [52, 53]. It incorporates the initial deconfined partonic phase, the final hadronic interactions, and the transition between these two phases of matter. AMPT model has four major components as described below.

- *Initialization:* The initial spatial and momentum distribution of partons, are generated by the

HIJING model [54]. Multiple scatterings among incoming nucleons are treated in the framework of eikonal formalism. The hard and soft components of particle production are respectively modeled by the formation of energetic minijet partons and soft string excitations. The differential cross-section of the produced mini-jet partons and excited strings are first calculated for pp collisions and are then converted into p+A and A+A collisions by using the in-built Glauber model [53, 54].

- *Transport of partons:* The produced partons are propagated to the Zhang's Parton Cascade (ZPC) model, where the Boltzmann transport equation for partons is solved via cascade method [55]. In the string-melting version of AMPT, all excited strings are converted into hadrons and then decomposed further into their constituent quarks [56]. These partons are then combined with the mini-jet partons and evolve through the ZPC model via two-body elastic parton scatterings [53].
- *Hadronization:* The transported partons are then hadronized using either the default mode or the string melting mode of AMPT. In the default mode, the transported partons are combined with their parent strings via the Lund string fragmentation model and then the strings get converted into hadrons [57]. In the string melting mode, transported partons are combined to form hadrons through a quark coalescence mechanism [56, 58]. In this model, a quark and an anti-quark sharing a close phase-space combine to form a meson while the three nearest quarks combine into baryons [53, 58].
- *Hadron transport:* Evolution of the resulting hadronic matter is described via hadron cascade, which is based on a relativistic transport (ART) model [59, 60]. The produced hadrons go through a final evolution via baryon-baryon, meson-baryon, and meson-meson scatterings and decays [53].

As the quark coalescence mechanism for hadronization implemented in the string melting version of AMPT explains the particle p_T spectra and flow at intermediate- p_T , we use the string melting mode of AMPT (version 2.26t9b) for this study [16, 38, 61–67]. For this study, in AMPT, we take the partonic scattering cross-section to be $\sigma_{gg} = 3$ mb and the value of strong coupling constant as $\alpha_s = 0.33$. The Lund symmetric splitting function parameters are set as $a = 0.3$ and $b = 0.15$ [42]. The parton screening mass in the ZPC model is fixed to $\mu = 2.265$ fm $^{-1}$. With the above-mentioned settings in AMPT, we simulate p-O and p-C collisions at $\sqrt{s_{NN}} = 9.9$ TeV.

Since the impact parameter (b), the number of participants (N_{part}), and the number of binary collisions (N_{coll}) cannot be directly measured in experiments, we resort to Glauber model estimations for the same [68,

69]. Using the publicly available MC Glauber code (TGlauberMC-3.2) [69], the impact parameter distribution is sliced to obtain the required centralities of collision. We have also modified the in-built HIJING model in AMPT to incorporate SOG and α -cluster nuclear density profiles for both ^{16}O and ^{12}C nuclei. Due to the unavailability of experimental data for p-O and p-C collisions at the LHC, we tune the AMPT model parameters by comparing them with that of the p-Pb system. A detailed description of the parameter tuning is provided in the Appendix.

B. Nuclear density profiles

This study implements two different nuclear density profiles for the ^{12}C and ^{16}O nuclei, which are α -cluster type geometrical distribution and a model-independent Sum of Gaussians type nuclear density profile. Here, the technical details regarding the implementation of the two density profiles are discussed.

1. Sum Of Gaussians (SOG) density profile

To represent the nuclear charge density and extract charge density parameters in a model-independent fashion as approximated in experiments, one fits the nuclear densities with a sum of Gaussian functions (SOG) [70, 71]. SOG can accurately represent complex nuclear densities by exploiting the parameters of individual Gaussian functions, which makes SOG applicable to a broad list of nuclei. SOG can produce smooth and continuous descriptions of the nuclear density profiles, consequently simplifying many theoretical calculations due to the well-known properties of the Gaussian distribution function. In addition, SOG can produce a more realistic and precise description of the nuclear profiles as compared to the traditional uniform density or a Woods-Saxon description of the nucleus [70]. In this study, we use the sum of two Gaussian functions to simulate ^{12}C and ^{16}O nuclear profiles. The SOG nuclear charge density ($\rho(r)$) as a function of radial distance (r) is expanded as,

$$\rho(r) = C_1 e^{-a_1 r^2} + C_2 e^{-a_2 r^2}. \quad (1)$$

Here, the coefficients C_1 , C_2 , a_1 , and a_2 for the respective nuclei are obtained from Ref. [70]. Due to the rapid decrease of the Gaussian tail, the values of the charge density at various radii ($\rho(r)$) are advantageously decoupled. Table I shows the parameters of SOG that have been considered in this study to simulate the ^{12}C and ^{16}O nuclei.

TABLE I. Parameters of Sum of Gaussians nuclear density profile chosen for ^{12}C and ^{16}O nucleus [70].

Nucleus	C_1	C_2	a_1	a_2
Carbon (^{12}C)	-0.162	0.340	0.554	0.280
Oxygen (^{16}O)	-0.539	0.729	0.407	0.300

2. α -clustered nuclear geometry

The ^4He nucleus consisting of a pair of protons and a pair of neutrons is known as the α -particle. As discussed earlier, nucleons of certain light nuclei can cluster into groups of α -particles forming a stable geometrical shape. For this, the nuclei should have $4n$ (n is a positive integer) number of nucleons. In ^{12}C , three such α -particles cluster into forming an equilateral triangle, whereas in ^{16}O , four α -particles cluster into a regular tetrahedral arrangement. This α -cluster geometry is believed to account for the additional stability of the nucleus. In our study, for the first time, we have implemented such α -cluster geometry for ^{12}C and ^{16}O nuclei to study the initial-state effects in particle production through p-C and p-O collisions at the LHC. The technical details of the implementation of α -cluster structure for ^{12}C and ^{16}O are discussed below.

• Tetrahedral geometry for ^{16}O

For the ^{16}O nucleus, four α -particles are situated at the four vertices of a regular tetrahedron with side length 3.42 fm, which makes the rms radius of ^{16}O to be 2.699 fm [16, 38, 39]. One can visualize the nucleons inside the ^{16}O nuclei as depicted in Fig. 1. Nucleons inside the α -particle are sampled using the following Woods-Saxon density profile in terms of a three-parameter Fermi (3pF) distribution,

$$\rho(r) = \frac{\rho_0 \left(1 + w \left(\frac{r}{r_0}\right)^2\right)}{1 + \exp\left(\frac{r-r_0}{a}\right)}. \quad (2)$$

Here, $\rho(r)$ is the nuclear charge density at a radial distance r from the center of the nucleus. r_0 refers to the mean radius of the nucleus, w is the nuclear deformation parameter, and a is the skin depth. The values of these parameters are chosen for the ^4He nucleus as $r_0 = 0.964$ fm, $w = 0.517$, and $a = 0.322$ fm, which corresponds to the rms radius of 1.676 fm for the α -particle. To include a finite volume effect for each nucleon, the minimum separation distance between any two nucleons is set to be 0.4 fm. The spatial orientation of the tetrahedron is randomized before each collision for both the target and projectile nuclei.

• Triangular geometry for ^{12}C

For the ^{12}C nucleus, three α -particles arrange themselves at the corners of an equilateral triangle

of side length 3.10 fm [49, 72]. One can visualize the nucleons inside the ^{12}C nuclei as depicted in Fig. 1. These parameters lead to a rms radius of 2.47 fm for the ^{12}C nucleus. The nucleons inside the α -particles are sampled using a similar procedure as discussed above.

C. Two-particle cumulants

Azimuthal anisotropy is one of the key observables that can characterize the medium formed in relativistic heavy-ion collisions. The asymmetric pressure gradient created in the medium due to the initial spatial anisotropy of the nuclear overlap region can transform into the final state momentum space azimuthal anisotropy. This is also known as the anisotropic flow. The anisotropic flow can be quantified as the coefficients of Fourier expansion of the azimuthal momentum distribution of the final-state particles as follows [73],

$$\frac{dN}{d\phi} = \frac{1}{2\pi} \left(1 + \sum_{n=1}^{\infty} 2v_n \cos[n(\phi - \psi_n)]\right). \quad (3)$$

Here, ϕ is the azimuthal angle, ψ_n is the n th harmonic event-plane angle, and v_n characterize the n th-order anisotropic flow coefficient. v_1 stands for the directed flow, v_2 for elliptic flow and v_3 characterises the triangular flow, and so on. One can estimate the anisotropic flow of different orders using the following expression [73],

$$v_n = \langle \cos[n(\phi - \psi_n)] \rangle. \quad (4)$$

Here, $\langle \dots \rangle$ represents the average over all particles in an event. The estimation of anisotropic flow coefficients from Eq. (4) is not slick since it requires ψ_n whose measurement is not trivial in experiments. In addition, the flow coefficients estimated using Eq. (4) are prone to non-flow effects, such as contributions from jets, and short-range resonance decays. These effects are more pronounced in small collision systems. Thus, to avoid these issues, multi-particle cumulant method is prescribed to estimate the anisotropic flow coefficients. In this method, one does not require the information of ψ_n and the non-flow effects can also be significantly reduced by implementing a proper relative pseudorapidity ($\Delta\eta$) cut between the particles.

In this study, the anisotropic flow coefficients are estimated using a two-particle Q -cumulant method. In this method, the two-particle azimuthal correlations are expressed in terms of a Q -vector as follows [74–76],

$$Q_n = \sum_{j=1}^M e^{in\phi_j}. \quad (5)$$

Here, M is the multiplicity of the event, and ϕ_j is the azimuthal angle of j th hadron. The index ‘ j ’ runs over

TABLE II. The impact parameter, average number of nucleon-nucleon binary collisions and average number of nucleon participants for different density profiles and in different centrality classes for p-O collisions at $\sqrt{s_{\text{NN}}} = 9.9$ TeV. Centrality selection is done through geometrical slicing, *i.e.*, from the impact parameter obtained from the Glauber model.

p-O	SOG				α-cluster			
	Centrality (%)	b_{min} (fm)	b_{max} (fm)	$\langle N_{\text{coll}} \rangle \pm \text{rms}$	$\langle N_{\text{part}} \rangle \pm \text{rms}$	b_{min} (fm)	b_{max} (fm)	$\langle N_{\text{coll}} \rangle \pm \text{rms}$
0-5	0	0.81	6.64 ± 2.12	7.64 ± 2.12	0	0.80	5.65 ± 1.64	6.65 ± 1.64
5-10	0.81	1.15	5.94 ± 1.92	6.94 ± 1.92	0.80	1.14	5.30 ± 1.64	6.30 ± 1.64
10-20	1.15	1.63	5.00 ± 1.75	6.00 ± 1.75	1.14	1.61	4.78 ± 1.56	5.78 ± 1.56
20-30	1.63	2.00	3.96 ± 1.56	4.96 ± 1.56	1.61	1.97	4.08 ± 1.40	5.08 ± 1.40
30-40	2.00	2.32	3.16 ± 1.40	4.16 ± 1.40	1.97	2.28	3.43 ± 1.27	4.43 ± 1.27
40-50	2.32	2.60	2.54 ± 1.24	3.54 ± 1.24	2.28	2.56	2.84 ± 1.15	3.84 ± 1.15
50-60	2.60	2.89	2.08 ± 1.06	3.08 ± 1.06	2.56	2.82	2.37 ± 1.03	3.37 ± 1.03
60-70	2.89	3.18	1.73 ± 0.87	2.73 ± 0.87	2.82	3.08	1.99 ± 0.90	2.99 ± 0.90
70-100	3.18	7.50	1.26 ± 0.54	2.26 ± 0.54	3.08	5.38	1.43 ± 0.65	2.43 ± 0.65

TABLE III. The impact parameter, average number of nucleon-nucleon binary collisions and average number of nucleon participants for different density profiles and in different centrality classes for p-C collisions at $\sqrt{s_{\text{NN}}} = 9.9$ TeV. Centrality selection is done through geometrical slicing, *i.e.*, from the impact parameter obtained from the Glauber model.

p-C	SOG				α-cluster			
	Centrality (%)	b_{min} (fm)	b_{max} (fm)	$\langle N_{\text{coll}} \rangle \pm \text{rms}$	$\langle N_{\text{part}} \rangle \pm \text{rms}$	b_{min} (fm)	b_{max} (fm)	$\langle N_{\text{coll}} \rangle \pm \text{rms}$
0-5	0	0.76	5.49 ± 1.84	6.49 ± 1.84	0	0.71	6.05 ± 1.89	7.05 ± 1.89
5-10	0.76	1.08	4.91 ± 1.69	5.91 ± 1.69	0.71	1.00	5.46 ± 1.68	6.46 ± 1.68
10-20	1.08	1.53	4.14 ± 1.53	5.14 ± 1.53	1.00	1.42	4.70 ± 1.54	5.70 ± 1.54
20-30	1.53	1.90	3.25 ± 1.34	4.25 ± 1.34	1.42	1.74	3.85 ± 1.38	4.85 ± 1.38
30-40	1.90	2.18	2.61 ± 1.18	3.61 ± 1.18	1.74	2.02	3.14 ± 1.27	4.14 ± 1.27
40-50	2.18	2.46	2.15 ± 1.03	3.15 ± 1.03	2.02	2.27	2.60 ± 1.15	3.60 ± 1.15
50-60	2.46	2.74	1.80 ± 0.88	2.80 ± 0.88	2.27	2.51	2.18 ± 1.02	3.18 ± 1.02
60-70	2.74	3.03	1.54 ± 0.73	2.54 ± 0.73	2.51	2.76	1.85 ± 0.90	2.85 ± 0.90
70-100	3.03	7.44	1.19 ± 0.45	2.19 ± 0.45	2.76	5.86	1.36 ± 0.62	2.36 ± 0.62

TABLE IV. Centrality dependence of average charged-particle multiplicity density for various nuclear profiles in p-O and p-C collisions at $\sqrt{s_{\text{NN}}} = 9.9$ TeV in the range $|\eta_{\text{lab}}| < 0.5$

Centrality (%)	p-O		p-C	
	$\langle dN_{ch}/d\eta \rangle_{\text{SOG}}$	$\langle dN_{ch}/d\eta \rangle_{\alpha\text{-cluster}}$	$\langle dN_{ch}/d\eta \rangle_{\text{SOG}}$	$\langle dN_{ch}/d\eta \rangle_{\alpha\text{-cluster}}$
0-5	35.56 ± 0.02	26.02 ± 0.02	30.43 ± 0.02	25.26 ± 0.04
5-10	30.97 ± 0.02	25.03 ± 0.02	26.33 ± 0.02	24.14 ± 0.03
10-20	25.48 ± 0.02	23.44 ± 0.02	21.92 ± 0.02	22.29 ± 0.04
20-30	19.91 ± 0.02	20.92 ± 0.02	17.28 ± 0.02	19.71 ± 0.02
30-40	15.88 ± 0.01	18.00 ± 0.02	13.97 ± 0.02	17.12 ± 0.04
40-50	12.94 ± 0.01	15.45 ± 0.02	11.55 ± 0.02	14.71 ± 0.02
50-60	10.65 ± 0.01	13.02 ± 0.03	9.66 ± 0.01	12.48 ± 0.03
60-70	8.80 ± 0.01	10.67 ± 0.03	8.05 ± 0.01	10.47 ± 0.03
70-100	5.61 ± 0.01	5.89 ± 0.02	5.28 ± 0.01	5.03 ± 0.46

all the charged hadrons. The single-event average two-particle azimuthal correlations are estimated using the following expression,

$$\langle 2 \rangle = \frac{|Q_n|^2 - M}{M(M-1)}. \quad (6)$$

Using Eq. (6), one can estimate the two-particle cumu-

lants as follows,

$$c_n\{2\} = \langle \langle 2 \rangle \rangle = \frac{\sum_{i=1}^{N_{\text{ev}}} (W_{\langle 2 \rangle})_i \langle 2 \rangle_i}{\sum_{i=1}^{N_{\text{ev}}} (W_{\langle 2 \rangle})_i}. \quad (7)$$

Here, $\langle \langle \rangle \rangle$ denotes the average over all particles over all the events. N_{ev} is the total number of events used for the calculations, and $(W_{\langle 2 \rangle})_i$ is the weight factor for the i th event which takes into account the number of different

two-particle combinations in an event with multiplicity M . $W_{\langle 2 \rangle}$ can be estimated as follows,

$$W_{\langle 2 \rangle} = M(M - 1). \quad (8)$$

One can obtain the value of event-averaged reference flow with the two-particle cumulants using the following expression,

$$v_n\{2\} = \sqrt{c_n\{2\}}. \quad (9)$$

However, to estimate the differential flow of the Particles Of Interest (POIs), one can define p_n and q_n vectors with specific kinematic cuts as follows,

$$\begin{aligned} p_n &= \sum_{j=1}^{m_p} e^{in\phi_j}, \\ q_n &= \sum_{j=1}^{m_q} e^{in\phi_j}, \end{aligned} \quad (10)$$

where, m_p is the total number of particles labeled as POIs, and m_q is the total number of particles tagged both as reference flow particles (RFP) and POI. One can estimate the single-event averaged differential two-particle azimuthal correlation using the following expression,

$$\langle 2' \rangle = \frac{p_n Q_n^* - m_q}{m_p M - m_q}. \quad (11)$$

Finally, the differential flow, $v_2(p_T)$, can be estimated using the following equation,

$$v_n\{2\}(p_T) = \frac{d_n\{2\}}{\sqrt{c_n\{2\}}}. \quad (12)$$

Here, $d_n\{2\}$ is the differential n^{th} -order cumulant given as,

$$d_n\{2\} = \langle \langle 2' \rangle \rangle = \frac{\sum_{i=1}^{N_{\text{ev}}} (w_{\langle 2' \rangle})_i \langle 2' \rangle_i}{\sum_{i=1}^{N_{\text{ev}}} (w_{\langle 2' \rangle})_i}. \quad (13)$$

The weight factor, $w_{\langle 2' \rangle}$, is given by,

$$w_{\langle 2' \rangle} = m_p M - m_q. \quad (14)$$

Unfortunately, the $v_n(p_T)$ obtained from Eq. (12) possesses contributions from non-flow effects which can be suppressed by appropriate kinematic cuts. For example, one can introduce a pseudorapidity gap between the particles in the two-particle Q -cumulant method [76]. Consequently, the whole event is divided into two sub-events, A and B , which are separated by a $|\Delta\eta|$ gap. This modifies Eq. (6) as,

$$\langle 2 \rangle_{\Delta\eta} = \frac{Q_n^A \cdot Q_n^{B*}}{M_A \cdot M_B}. \quad (15)$$

Here, Q_n^A and Q_n^B are the flow vectors from sub-events A and B , respectively. M_A and M_B are the multiplicities corresponding to the sub-events A and B , respectively.

The two-particle Q -cumulant with a $|\Delta\eta|$ gap is given by,

$$c_n\{2, |\Delta\eta|\} = \langle \langle 2 \rangle \rangle_{\Delta\eta} \quad (16)$$

where, one can estimate $\langle \langle 2 \rangle \rangle_{\Delta\eta}$ by using $\langle 2 \rangle_{\Delta\eta}$ from Eq. (15) with $M_A \cdot M_B$ as the event weights. If we select RFP from one sub-event and POIs from another to estimate the differential flow with a pseudorapidity gap, there is no overlap between POIs and RFP. This modifies Eq. (11) as,

$$\langle 2' \rangle_{\Delta\eta} = \frac{p_{n,A} Q_{n,B}^*}{m_{p,A} M_B}. \quad (17)$$

Now, one can obtain the two-particle differential cumulant by taking an event average over $\langle 2' \rangle_{\Delta\eta}$ from Eq. (17) with an event weight factor $m_{p,A} M_B$. Thus, the two-particle differential cumulant is given by,

$$d_n\{2, |\Delta\eta|\} = \langle \langle 2' \rangle \rangle_{\Delta\eta}. \quad (18)$$

Finally, the two-particle differential flow coefficient can be estimated using the following equation,

$$v_n\{2, |\Delta\eta|\}(p_T) = \frac{d_n\{2, |\Delta\eta|\}}{\sqrt{c_n\{2, |\Delta\eta|\}}}. \quad (19)$$

To estimate the anisotropic flow coefficients, the multi-particle Q -cumulants method is adopted in many experiments [76–78]. In this study, p_T differential second- and third-order flow coefficients, v_2 and v_3 , are estimated using the above equations by setting the $n = 2$ and 3 , respectively. To estimate the anisotropic flow coefficients, we use all the charged hadrons within the pseudorapidity region, $|\eta_{\text{lab}}| < 2.5$. The RFP are charged hadrons selected within $|\eta_{\text{lab}}| < 2.5$ and $0.2 < p_T < 5.0$ GeV/c. In addition, to reduce the non-flow effects from the two-particle Q -cumulant method, we use a pseudorapidity gap, $|\Delta\eta| > 1.0$, in the two-subevent method.

III. RESULTS AND DISCUSSIONS

In this section, we begin with a comparison of transverse momentum (p_T) and pseudorapidity (η) spectra for the final-state charged particles followed by a discussion on the participant eccentricity (ϵ_2) and triangularity (ϵ_3) in p-C and p-O collisions at $\sqrt{s_{\text{NN}}} = 9.9$ TeV using AMPT. Then, we discuss the centrality and p_T dependence of elliptic flow (v_2) and triangular flow (v_3), and v_3/v_2 as a function of collision centrality. Finally, the results for v_2/ϵ_2 and v_3/ϵ_3 as a function of collision centrality have been reported. All these results include a comparison between the SOG and α -cluster type density profiles for the ^{12}C and ^{16}O nucleus.

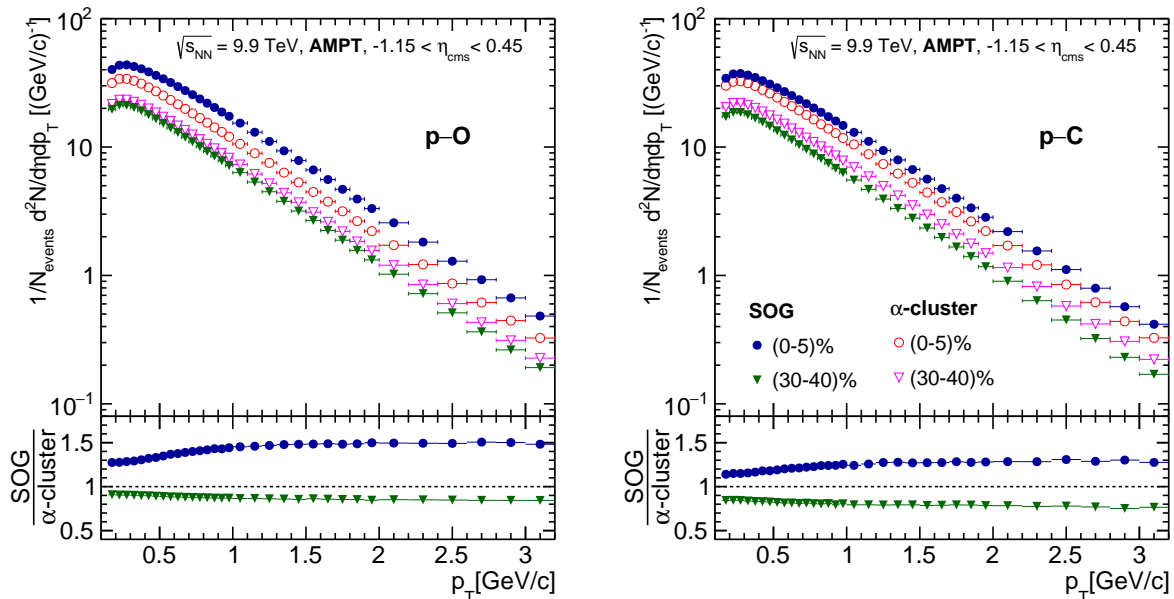


FIG. 2. (Color online) Upper panel shows p_T -spectra of all charged particles for different nuclear density profiles in p-O (left) and p-C (right) collisions at $\sqrt{s_{NN}} = 9.9$ TeV for (0-5)% and (30-40)% centrality classes. The ratios of p_T spectra of SOG to α -cluster density profile for respective centrality classes are shown in the lower panel.

As discussed earlier, we define the collision centrality by the geometrical slicing of the impact parameter (b) distributions for p-C and p-O collisions at $\sqrt{s_{NN}} = 9.9$ TeV. Table II and III shows the impact parameter values against each centrality class, along with the mean number of binary collisions ($\langle N_{coll} \rangle$) and average number of participants ($\langle N_{part} \rangle$) for both SOG and α -cluster type nuclear density profiles in p-O and p-C collisions at $\sqrt{s_{NN}} = 9.9$ TeV, respectively. These values are obtained from the Glauber model simulation. For a given centrality class, the upper-cut on the impact parameter (b_{max}) is always smaller for the case of α -cluster nuclear density profile compared to the SOG for both p-C and p-O collision systems. For the central p-O collisions (up to (10-20)%), $\langle N_{part} \rangle$ and $\langle N_{coll} \rangle$ are higher for the SOG density profile than the α -cluster nuclear distribution. However, beyond (20-30)% centrality class, in mid-central and peripheral collisions, $\langle N_{part} \rangle$ and $\langle N_{coll} \rangle$ values are higher for the case of α -cluster as compared to the SOG. In contrast, for the p-C collisions, $\langle N_{part} \rangle$ and $\langle N_{coll} \rangle$ values for α -cluster is always higher than the SOG type density profile irrespective of the centrality of the collision.

Since the collision systems are asymmetric, the center-of-mass frame of p-O or p-C collisions do not coincide with the laboratory frame. Thus, the shift in rapidity of the center-of-mass frame (y_{cms}) from the lab frame (y_{lab}) needs to be included. For asymmetric collisions, the shift in rapidity (Δy) can be expressed in terms of the atomic number (Z) and mass number (A) of the colliding nuclei

as,

$$\Delta y = |y_{lab} - y_{cms}| = \frac{1}{2} \ln [Z_1 A_2 / Z_2 A_1]. \quad (20)$$

The subscripts 1 and 2 denote the projectile and target nuclei, respectively. For both p-O and p-C collisions, the rapidity shift is estimated to be $\Delta y = 0.346$ units in the direction of the proton beam. As a result, a detector coverage of $|\eta_{lab}| < 0.8$ would imply the nucleon-nucleon c.m.s to be roughly $-1.15 < \eta_{cms} < 0.45$. Table IV shows the mean charged particle multiplicity density ($\langle dN_{ch}/d\eta \rangle$) in $|\eta_{lab}| < 0.5$ as a function of collision centrality in p-O and p-C collisions for α -clustered and SOG nuclear density profiles. One finds that $\langle dN_{ch}/d\eta \rangle$ is higher for the SOG case for both p-O and p-C collisions for the central collisions, while towards mid-central and peripheral collisions, the multiplicity density is higher for the α -cluster case.

A. Transverse momentum (p_T) and pseudorapidity (η) distributions

Figure 2 shows the event normalized p_T -spectra for unidentified charged hadrons in $|\eta_{lab}| < 0.8$ for central (0-5)% and mid-central (30-40)% p-O (left), p-C (right) collisions at $\sqrt{s_{NN}} = 9.9$ TeV using AMPT. The p_T spectra include the cases for the two nuclear density profiles considered in this study, *i.e.*, the SOG and the α -cluster. For the most central p-O and p-C collisions, the charged particle yield is higher for the case of SOG as compared to

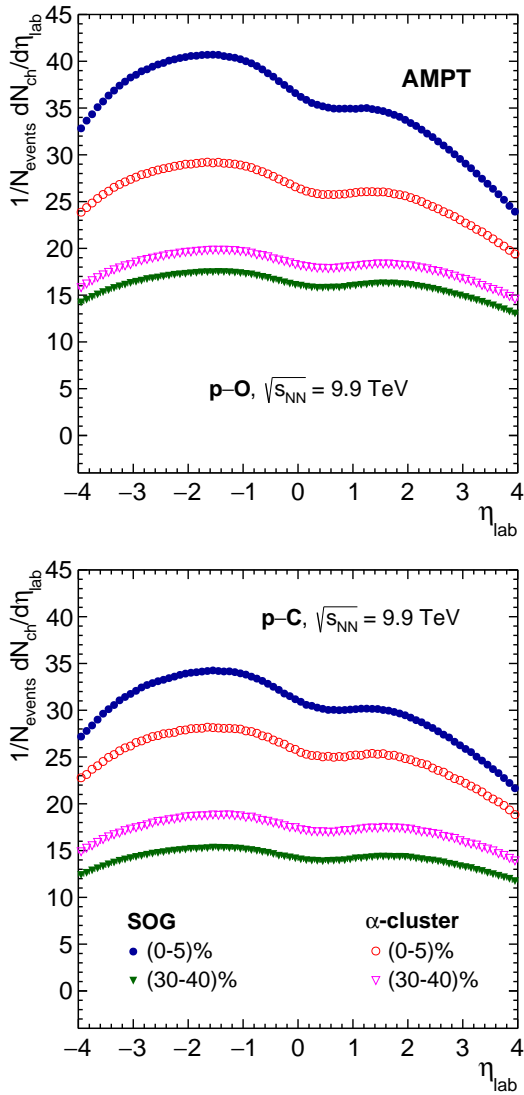


FIG. 3. (Color online) η -spectra of charged particles ($p_T > 0.15$ GeV/c) for different nuclear density profiles in p-O (upper) and p-C (lower) collisions at $\sqrt{s_{NN}} = 9.9$ TeV for (0–5)% and (30–40)% centrality classes.

the α -cluster density profile. This enhancement of yield for the SOG density profile for the most central collisions is larger in p-O collisions compared to the same centrality in p-C collisions. In contrast, an opposite trend is observed for the mid-central collisions, where the charged particle yield is enhanced for α -cluster density profile compared to SOG. This is also consistent with the results of $\langle dN_{ch}/d\eta \rangle$ shown in Table IV. On the bottom panels of Fig. 2, the ratio of p_T spectra of SOG to α -cluster type density profile has been shown for both collision systems. The ratios show a hardening of p_T spectra in the most central collisions for the SOG density profile compared to the α -cluster case. On the other hand, for the mid-central collisions, the SOG type density profile produces a slightly softer p_T -spectra than α -cluster density profile.

These effects of hardening in the central and softening in the peripheral collisions for the SOG density profile than the α -cluster density profile are significantly prominent in p-O than in p-C collisions [79, 80]. In hydrodynamics, the hardening of p_T spectra is attributed to the collective transverse flow generated due to hydrodynamic expansion [81]. As transport models like AMPT incorporate many of the experimentally measured collective features [16, 38, 61–67], a hardening of p_T spectra may hint to the presence of a hydrodynamically expanding system.

Figure 3 represents the η -spectra of all charged hadrons with $p_T > 0.15$ GeV/c for (0–5)% and (30–40)% centrality classes in p-O (upper) and p-C (lower) collisions at $\sqrt{s_{NN}} = 9.9$ TeV for SOG and α -clustered density profiles. One can observe a similarity in terms of collision centrality and nuclear density profile dependence of charged particle yield between Fig. 2 and 3. The yield in the most central p-O and p-C collisions is higher for the SOG nuclear density profile as compared to the clustered geometry of the nucleons. However, in the mid-central collisions, the yield is higher for α -clustered nuclear density profile as compared to the SOG case.

The double-peaks appearing in the pseudorapidity distribution seem to be symmetric around $\eta = 0$ towards peripheral p-O and p-C collisions, which is similar to pp collisions, possibly due to their similarity in geometry [82]. In other words, due to the smaller number of participants in the mid-central and peripheral p-O and p-C collisions, the scenario becomes equivalent to pp collisions with $\langle N_{part} \rangle \simeq 2-4$. However, as we move towards the central collisions in asymmetric collision systems, the pseudorapidity distribution becomes progressively more asymmetric around $\eta = 0$, such that fewer particles are produced in the direction of the proton beam while there is a predominant emission from the participant nucleons of the heavier nucleus. Unlike A-A nuclear collisions, the scenario in p-A collisions is that of a single nucleon probing the nucleons of a target nucleus in a narrow cylinder [83]. In a central p-A collision, the projectile proton interacts with a denser volume of the target nucleus than in the case of a peripheral p-A collision. Consequently, the yield in the nucleus-beam-going direction will increase from peripheral to central collisions. As one can see in Fig. 3, the multitude of particles produced is higher in the oxygen- and carbon-going directions than in the proton-going direction for the most central p-O and p-C collisions, respectively. In addition, one observes a slightly higher asymmetry in the double-peak structure of pseudorapidity distribution in p-O collisions as compared to p-C collisions, presumably due to a denser ^{16}O nuclei. The effects are further enhanced for an SOG system as compared to α -cluster nuclear density profile, indicating that the core part of an SOG is slightly denser as compared to an α -cluster nuclear geometry. This observation is consistent with our observation in Table IV.

B. Eccentricity and triangularity

In non-central nuclear collisions, the geometry of the transverse nuclear overlap region is non-spherical (more like almond-shaped) and it has finite spatial anisotropy, which induces asymmetric pressure gradients in the medium. If the pressure gradient is strong, the spatial anisotropy in the initial state is transformed into azimuthal anisotropy in the momentum space of the final state particles through the collective expansion of the medium. The initial spatial anisotropy can be quantified in terms of eccentricity (ϵ_2) and triangularity (ϵ_3) of the participant nucleons. Eccentricity quantifies the extent to which the transverse overlap region is elliptical, and triangularity tells how triangular the transverse participant plane is. While eccentricity has a major contribution from the asymmetry in the collision geometry, triangularity can develop due to the event-by-event density fluctuations in the collision overlap region. In experiments, the measurement of ϵ_2 and ϵ_3 is nontrivial. However, Monte Carlo models like AMPT can provide the coordinates of the participant nucleons. Thus, one can quantify the spatial anisotropy, ϵ_n , using the following expression [84],

$$\epsilon_n = \frac{\sqrt{\langle r^n \cos(n\phi_{\text{part}}) \rangle^2 + \langle r^n \sin(n\phi_{\text{part}}) \rangle^2}}{\langle r^n \rangle}. \quad (21)$$

Here, r and ϕ_{part} are the polar coordinates of the participant nucleons in the transverse plane, and n denotes the order of spatial anisotropy, *i.e.*, ϵ_2 and ϵ_3 correspond to the second and third order spatial anisotropy, respectively. In Eq. (21), $\langle \dots \rangle$ denotes the average over all the participating nucleons in an event.

Although the initial state in A–A collisions can be characterized by the overall geometrical shape of the interaction region, the scenario becomes different as we come to p–A collision systems. In the latter, the number of participants is comparatively less than nucleus–nucleus collisions, and the system’s geometry grows sensitive to the proton’s size. In short, the eccentricity and triangularity of the source in proton-induced interactions are fluctuation-dominated, and the size of the system is dominated by the incoming proton [85]. The upper panels in Fig. 4 show the event-averaged eccentricity ($\langle \epsilon_2 \rangle$) and triangularity ($\langle \epsilon_3 \rangle$) as a function of centrality for p–O (left) and p–C (right) collisions at $\sqrt{s_{\text{NN}}} = 9.9$ TeV, and the ratio $\langle \epsilon_3 \rangle / \langle \epsilon_2 \rangle$ is plotted in the lower panels. It is observed that for the SOG density profile, $\langle \epsilon_2 \rangle$ increases linearly with an increase in centrality for both p–O and p–C collision systems. This trend is also quite similar to that of $\langle \epsilon_2 \rangle$ for the Woods-Saxon density profile in O–O collisions obtained using AMPT as can be in Ref. [16]. In A–A collisions, the reason for the increasing trend of $\langle \epsilon_2 \rangle$ with centrality is a growing elliptic geometry of the collision overlap region. However, this is not applicable for p–A collisions. In p–A collisions, the contributions from increasing fluctuations or decreasing matter density with

an increase in impact parameter towards the peripheral collisions can lead to a significant increase in eccentricity. On the other hand, the behavior of $\langle \epsilon_2 \rangle$ with an increase in collision centrality becomes much more interesting for the α -cluster case. Here, $\langle \epsilon_2 \rangle$ increases non-linearly till (20–30)% centrality and remains almost unaffected with the increase in centrality till (60–70)% centrality, and finally increases sharply for the (70–100)% centrality bin. Noticeably, this behavior of $\langle \epsilon_2 \rangle$ with an increase in collision centrality is similar for both p–O and p–C collisions for the α -cluster case. In addition, a similar observation for $\langle \epsilon_2 \rangle$ is made for O–O collisions with an α -cluster nuclear density profile using AMPT [16]. This observation indicates that even if the colliding nuclear species are the same, the distribution of nucleons within the colliding nuclei does play a major role in determining the initial spatial anisotropy of the collision overlap region. Further, a clustered nuclear structure shows a similar footprint for $\langle \epsilon_2 \rangle$ with varying centrality throughout p–O, p–C, and O–O collisions. Moreover, if we draw a comparison between the two collision systems, for a given collision centrality, the values of eccentricity are higher for p–C collisions than p–O collisions for both the density profiles. This is presumably because of a smaller system size in p–C collisions than in p–O collisions, which leads to a larger fluctuation in the participant nucleon distribution and a larger value of $\langle \epsilon_2 \rangle$ for p–C collisions compared to p–O collisions.

The variation of $\langle \epsilon_3 \rangle$ as a function of collision centrality appears slightly different for p–O and p–C collisions in Fig. 4. $\langle \epsilon_3 \rangle$ increases with centrality, almost in a similar fashion for both the density profiles in p–C collisions. In contrast, in p–O collisions, $\langle \epsilon_3 \rangle$ for α -cluster density profile dominates over that of SOG density profile in the most central case, drops in the mid-central collisions followed by a rise in the peripheral cases. As this pattern of $\langle \epsilon_3 \rangle$ for α -cluster density profile in p–O collisions is similar to that of $\langle \epsilon_3 \rangle$ in Ref. [16] for O–O collisions, this trend could be attributed specifically to the presence of an α -clustered ^{16}O nucleus. Additionally, the complimentary trend between $\langle \epsilon_2 \rangle$ and $\langle \epsilon_3 \rangle$ in the case of α -cluster density profile for p–O system is worth noting. The ratio $\langle \epsilon_3 \rangle / \langle \epsilon_2 \rangle$ for the SOG density profile in both p–O and p–C collision systems show a very similar trend, which gradually decreases with increasing centrality and approaches unity ($\langle \epsilon_3 \rangle \simeq \langle \epsilon_2 \rangle$) for mid-central to peripheral collisions. This trend indicates that the spatial anisotropy in central p–A collisions have a larger contribution from event-by-event fluctuations as compared to the shape of the nuclear overlap region since $\langle \epsilon_3 \rangle / \langle \epsilon_2 \rangle > 1.0$. However, in the case of an α -cluster density profile, $\langle \epsilon_3 \rangle / \langle \epsilon_2 \rangle$ shows a sharp increase for the most central p–O collisions, which then decreases to unity towards mid-central collisions to rise again in peripheral collisions. This is once again consistent with the results for O–O collisions for α -cluster density profile using AMPT, as shown in Ref. [16]. This dominance of $\langle \epsilon_3 \rangle / \langle \epsilon_2 \rangle$ for the most central p–O collisions with the α -clustered profile is absent

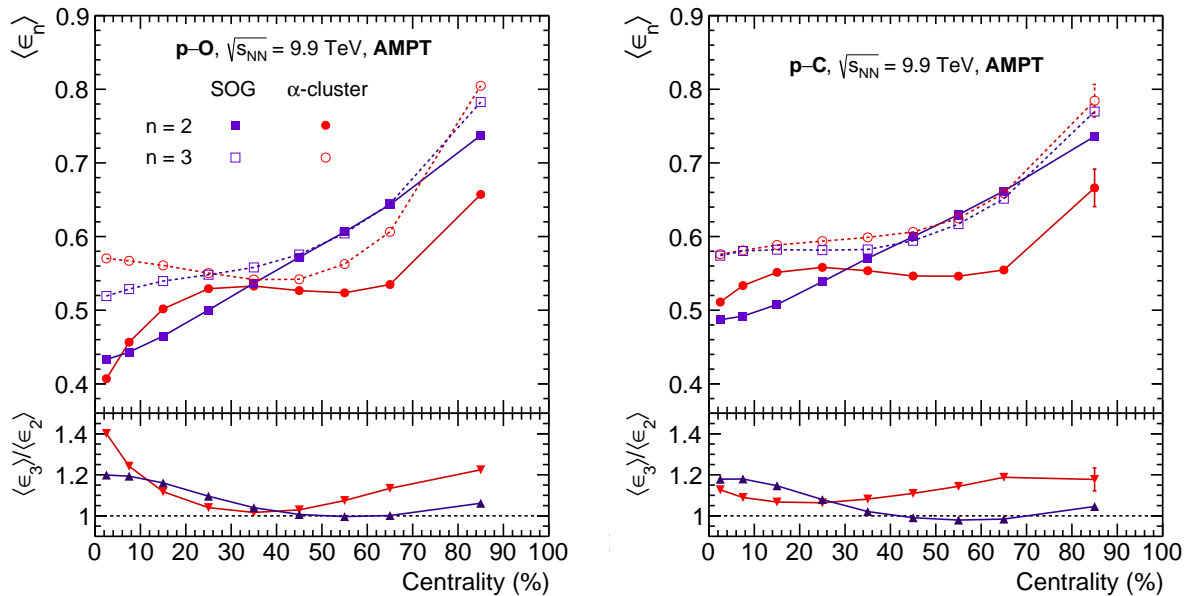


FIG. 4. (Color online) Centrality dependence of average eccentricity ($\langle \epsilon_2 \rangle$) and triangularity ($\langle \epsilon_3 \rangle$) for p-O (left) and p-C (right) collisions at $\sqrt{s_{NN}} = 9.9$ TeV using AMPT for SOG and α -cluster nuclear density profiles are shown in the upper panels. Lower panels shows the ratio $\langle \epsilon_3 \rangle / \langle \epsilon_2 \rangle$ as a function of centrality.

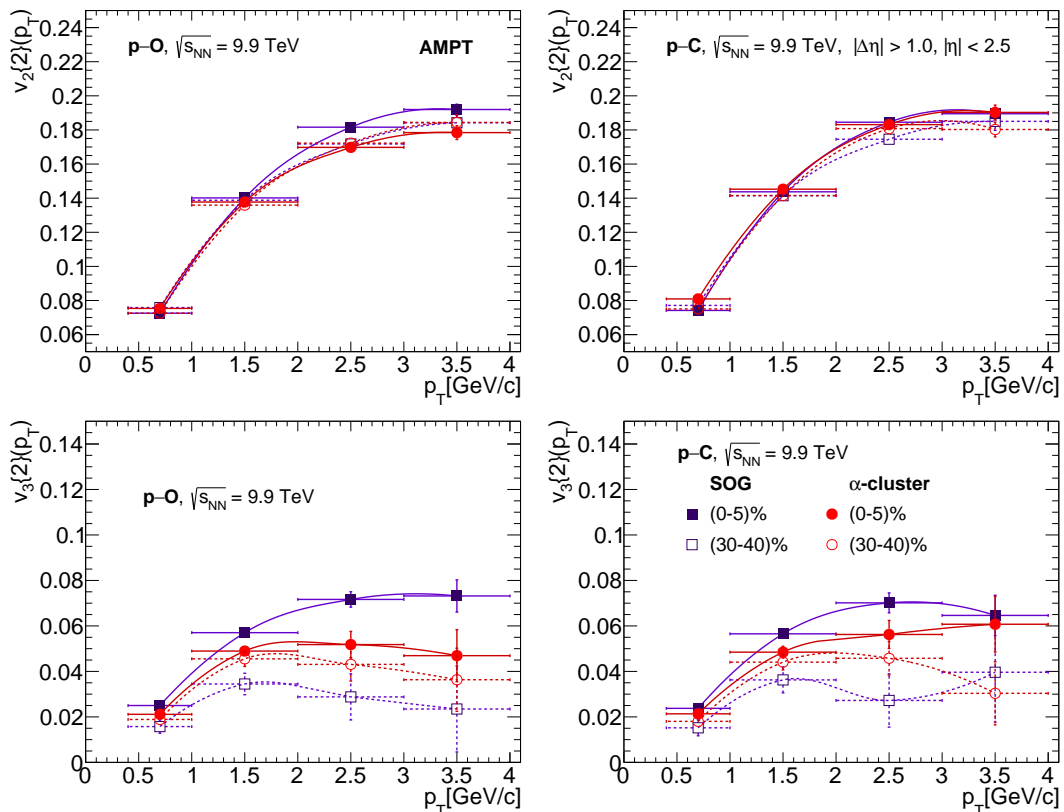


FIG. 5. (Color online) Elliptic flow (upper) and triangular flow (lower) of charged particles as a function of transverse momentum in p-O (left) and p-C (right) collisions at $\sqrt{s_{NN}} = 9.9$ TeV for SOG and α -cluster nuclear density profiles in (0-5)% and (30-40)% centrality classes.

in p-C collisions. This behavior may be attributed to the presence of an extra α -cluster in the oxygen nucleus

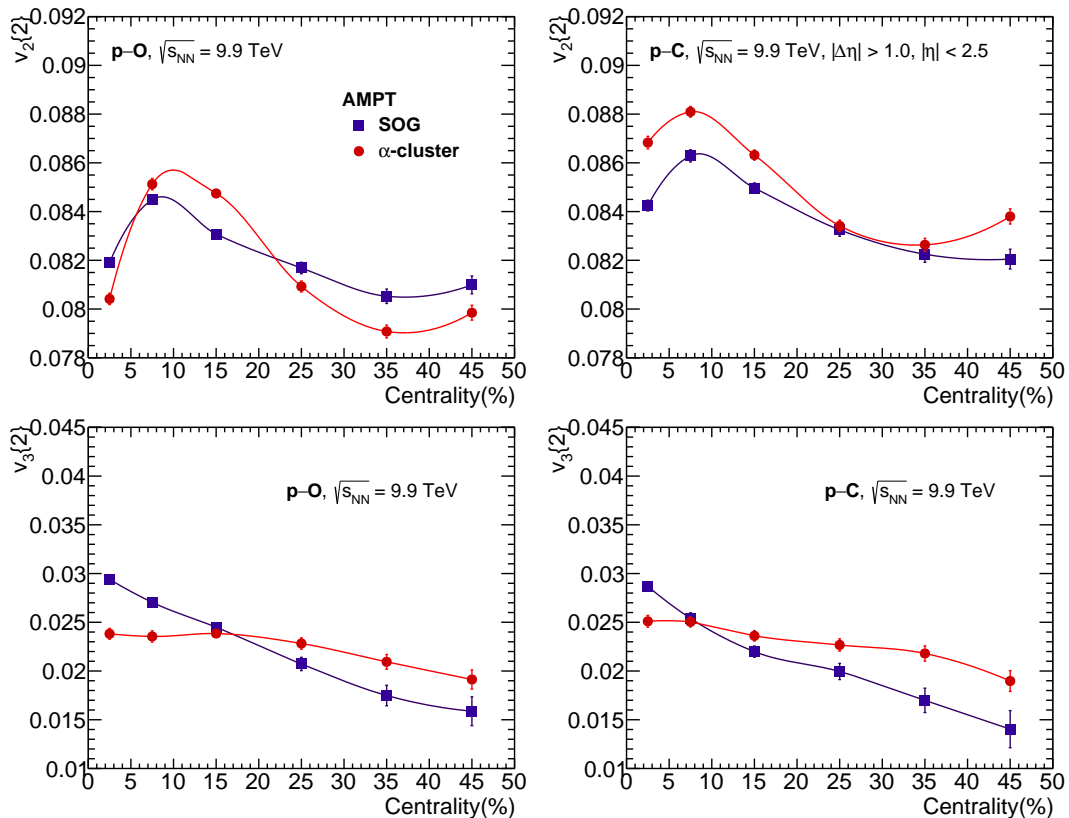


FIG. 6. (Color online) Centrality dependence of elliptic flow ($v_2\{2\}$) (upper) and triangular flow ($v_3\{2\}$) (lower) in p-O (left) and p-C (right) collisions at $\sqrt{s_{NN}} = 9.9$ TeV for SOG and α -cluster nuclear density profiles using AMPT model.

than in the carbon, which leads to an additional density fluctuation in the most central case for the p-O collisions resulting in a higher value of $\langle \epsilon_3 \rangle$.

C. Elliptic flow and triangular flow

Figure 5 represents p_T dependence of elliptic flow (upper) and triangular flow (lower) for all charged particles in $|\eta| < 2.5$ measured using two-particle Q -cumulant method for SOG and α -cluster nuclear density profiles in p-O (left) and p-C (right) collisions for (0-5)% and (30-40)% centrality bins, using AMPT model. $v_2\{2\}(p_T)$ increases at low- p_T , and becomes maximum towards the intermediate- p_T in both p-O and p-C collisions for both the nuclear density profiles. For (0-5)% and (30-40)% centrality classes shown here, $v_2\{2\}(p_T)$ in both p-O and p-C collisions are estimated to have almost similar values despite having a sizeable difference in the initial eccentricity for these two centrality bins. Again, for these centrality bins, the effect of the density profiles on the estimated $v_2\{2\}(p_T)$ is also very minimal. However, a clear distinction for the case of $v_3\{2\}(p_T)$ values are seen as a function of centrality and the choice of nuclear density profile.

Figure 6 shows the centrality dependence of elliptic

flow (upper) and triangular flow (lower) using the two-particle Q -cumulant method for SOG and α -cluster nuclear density profiles in p-O (left) and p-C (right) collisions at $\sqrt{s_{NN}} = 9.9$ TeV using AMPT. Interestingly, the SOG nuclear density profile shows a similar centrality dependence of $v_2\{2\}$ for both p-O and p-C collisions. Here, $v_2\{2\}$ rises from (0-5)% to (5-10)% centrality class followed by a smooth drop towards mid-central and peripheral collisions. However, one finds that $v_2\{2\}$ is slightly higher for p-C collisions as compared to p-O collisions which can be attributed to the higher value of $\langle \epsilon_2 \rangle$ for the p-C collisions as seen in Fig. 4.

Further, one observes a similar centrality dependence of $v_2\{2\}$ between p-O and p-C collisions with the α -cluster nuclear density profile. However, in p-O collisions, $v_2\{2\}$ for the α -cluster nuclear density profile is smaller in magnitude compared to the same in the SOG type nuclear density, excluding (05-20)% centrality class. Again, in p-O collisions, the crossing of $v_2\{2\}$ between α -cluster and SOG density profiles within (0-5)% and (5-10)% centrality class is consistent with the crossing of $\langle \epsilon_2 \rangle$ for both nuclear density profiles seen in Fig. 4. However, towards the mid-central and peripheral collisions, due to a smaller number of participants, the centrality dependence of $\langle \epsilon_2 \rangle$ might not be well reflected in the corresponding values of $v_2\{2\}$. In p-C collisions, $v_2\{2\}$ for

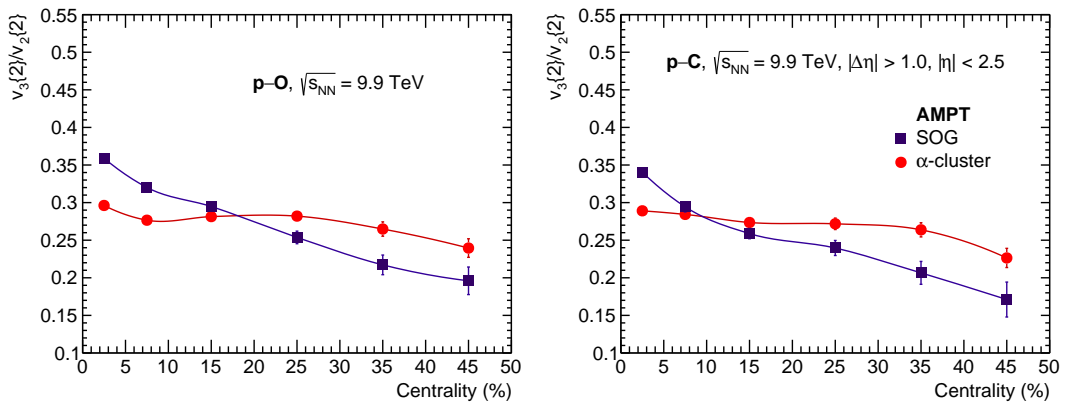


FIG. 7. (Color online) $v_3\{2\}/v_2\{2\}$ as a function of centrality in p-O (left) and p-C (right) collisions at $\sqrt{s_{NN}} = 9.9$ TeV for SOG and α -cluster nuclear density profiles from AMPT.

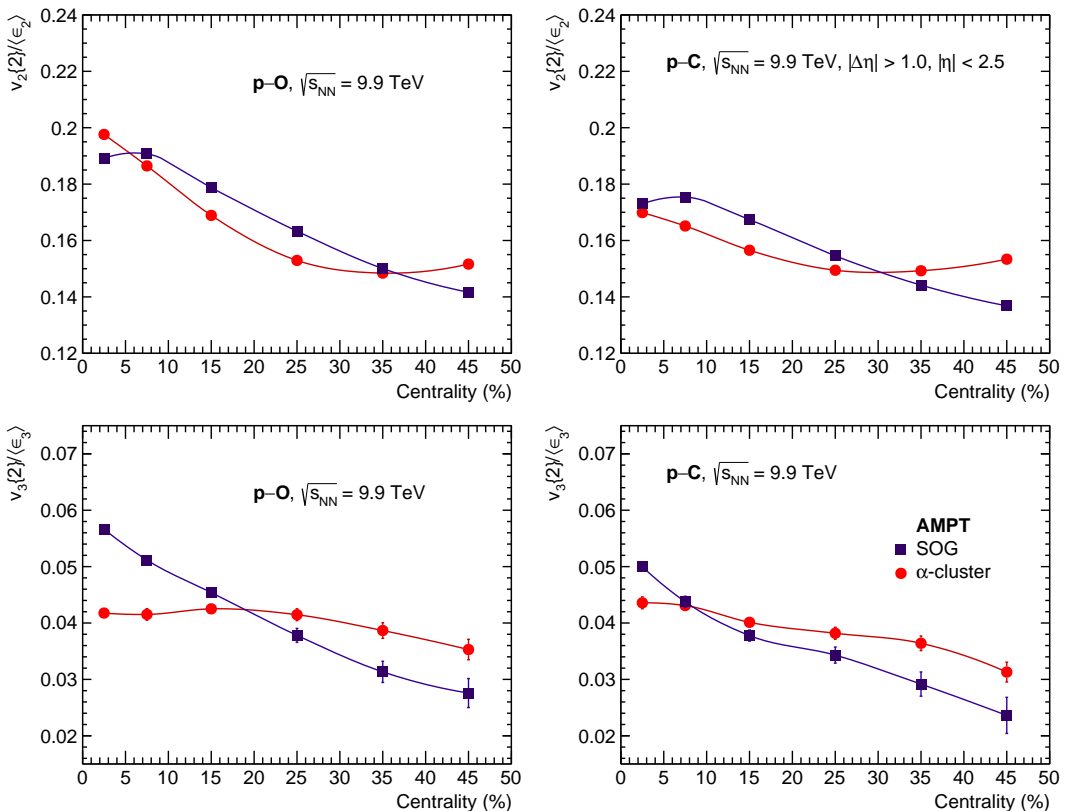


FIG. 8. (Color online) Ratio $v_2\{2\}/\langle\epsilon_2\rangle$ (upper) and $v_3\{2\}/\langle\epsilon_3\rangle$ (lower) as a function of centrality in p-O (left) and p-C (right) collisions at $\sqrt{s_{NN}} = 9.9$ TeV using AMPT for both SOG and α -cluster nuclear density profiles.

the α -cluster case is always higher than the corresponding values of $v_2\{2\}$ for the SOG case. This is consistent with corresponding $\langle\epsilon_2\rangle$ as shown in Fig. 4 till (20-30)% central collisions, but, for mid-central to peripheral collisions, the centrality dependence of $\langle\epsilon_2\rangle$ is not seen to be well reflected in the corresponding values of $v_2\{2\}$.

Moving to the centrality dependence of triangular flow ($v_3\{2\}$), as shown in the lower plots of Fig. 6, for both α -cluster and SOG nuclear density profiles, $v_3\{2\}$ is found

to decrease with an increase in centrality for both p-O and p-C collisions; however, the fall is found to be less steep for collisions involving α -clusters. Interestingly, one observes that while $\langle\epsilon_3\rangle$ shows an increasing trend towards the peripheral collisions, $v_3\{2\}$ shows a decreasing trend, which is expected in small collision systems like p-O and p-C collisions. Further, one may notice that $v_2\{2\}$ varies with a factor of maximum 8% between its lowest and highest values in both the nuclear profiles

and in both p–O and p–C collision systems. This weak dependence of elliptic flow coefficients is consistent with the experimental observation of elliptic flow in p–Pb [26], and p–Au [86–89] collisions. In contrast, for $v_3\{2\}$, one finds that the variation is more than 50% for SOG nuclear density profiles, while an α -cluster density profile shows a small centrality dependence in both p–O and p–C collisions.

Figure 7 shows the centrality dependence of ratio $v_3\{2\}/v_2\{2\}$ for SOG and α -cluster density profiles for p–O and p–C collisions. As one can see, the ratio is strictly less than one, which is consistent with the observations made in Pb–Pb and p–Pb collisions in experiments [26]. We observe that the trend for $v_3\{2\}/v_2\{2\}$ is very much identical to the trend for $\langle v_3 \rangle$, where a gradually decreasing ratio of SOG density profile is cut across in the mid-centralities by an almost flat curve of α -cluster density profile, for both the collision systems. This is because $v_2\{2\}$ has a smaller centrality dependence, whereas $v_3\{2\}$ is affected significantly with a change in collision centrality.

The ratio of v_n/ϵ_n can be considered as the hydrodynamic medium response to the initial spatial anisotropy. Figure 8 shows the centrality dependence of ratio $v_2\{2\}/\langle \epsilon_2 \rangle$ (upper) and $v_3\{2\}/\langle \epsilon_3 \rangle$ (lower) in p–O (left) and p–C (right) collisions at $\sqrt{s_{NN}} = 9.9$ TeV using AMPT for both SOG and α -cluster nuclear density profiles. Naively, one finds that the centrality dependence of $v_2\{2\}/\langle \epsilon_2 \rangle$ is nearly proportional to $1/\langle \epsilon_2 \rangle$ for both the nuclear density profiles in both p–O and p–C collisions. This is because $v_2\{2\}$ has a weak dependence on collision centrality (Fig. 6), whereas $\langle \epsilon_2 \rangle$ shows a relatively stronger centrality dependence, shown in Fig. 4. In contrast, we find an interesting observation of the centrality dependence of $v_3\{2\}/\langle \epsilon_3 \rangle$. The SOG nuclear density profiles show a decreasing behavior from central to mid-central collisions, indicating a significant impact of the system formed in the evolution of the anisotropic flow coefficient. Interestingly, for the α -cluster case, the ratio $v_3\{2\}/\langle \epsilon_3 \rangle$ is less sensitive to collision centrality in both p–O and p–C collisions. The sensitivity is even less for p–O collisions than for p–C collisions. This marks one of the significant observations in p–O and p–C collisions, which relates to the presence of a clustered geometry in ^{16}O and ^{12}C nuclei.

IV. SUMMARY

In summary, for the first time, we report a systematic study of the effect of the nuclear density profile through p–O and p–C collisions at the LHC. We study the transverse momentum (p_T) and pseudorapidity (η) spectra, eccentricity and triangularity, elliptic and triangular flow in p–O and p–C collisions at $\sqrt{s_{NN}} = 9.9$ TeV using AMPT with α -cluster type geometry and a model-independent Sum of Gaussians (SOG) type nuclear density profiles.

With the study of p_T and η spectra, the study estab-

lishes the differences in the yield for both the nuclear density profiles for different centrality classes. In addition, one finds a significant ϵ_n dependence on the collision centrality, where an α -cluster nuclear density profile maintains a similar qualitative behavior with an increase in collision centrality in p–O, p–C and O–O collisions. This is one of the important findings of this paper; although it can not be confronted in experiments, it retains significant importance in understanding the collision overlap region for an α -clustered geometry. Further, p–Pb collisions and the α -cluster nuclear density profile of p–O and p–C collisions show a weak dependence of triangular flow on collision centrality. In contrast, the triangular flow for the SOG density profile shows a strong centrality dependence for both p–O and p–C collision systems. Finally, for an α -cluster nuclear density profile, $v_3\{2\}/\langle \epsilon_3 \rangle$ has a small dependence on collision centrality where SOG nuclear profile shows a linear drop with an increase in collision centrality. This is one of the important findings of this paper and can be confronted in experiments in the upcoming p–O collisions.

ACKNOWLEDGEMENT

A.M.K.R. acknowledges the doctoral fellowships from the DST INSPIRE program of the Government of India. S.P. acknowledges the University Grants Commission (UGC), Government of India. The authors gratefully acknowledge the DAE-DST, Government of India funding under the mega-science project ‘‘Indian participation in the ALICE experiment at CERN’’ bearing Project No. SR/MF/PS-02/2021-IITI(E-37123).

APPENDIX

Figure 9 shows the comparison of transverse momentum spectra in minimum bias p–Pb collisions from AMPT with the ALICE measurements [90] at $\sqrt{s_{NN}} = 5.02$ TeV. In addition, we compare the transverse momentum spectra of minimum bias p–O (left) and p–C (right) collisions at $\sqrt{s_{NN}} = 9.9$ TeV. Due to a lack of experimental results for p–O and p–C collisions, we have first tuned AMPT for p–Pb collisions to the best possible match with minimum bias p_T -spectra from ALICE measurements for p–Pb collisions at $\sqrt{s_{NN}} = 5.02$ TeV. Further, we keep similar tuning of AMPT, as discussed in Section II, to simulate p–O and p–C collisions. One finds a fair agreement between AMPT and ALICE results for p–Pb collisions at $\sqrt{s_{NN}} = 5.02$ TeV, at $p_T > 3$ GeV/c. Similarly, the qualitative trends for p–O and p–C collisions from AMPT for both the nuclear density profiles match quite well with AMPT results for p–Pb collisions at $\sqrt{s_{NN}} = 5.02$ TeV.

Figure 10 shows the probability distribution of the radial position of the nucleons inside ^{12}C and ^{16}O nucleus. The nucleon probability distribution considering an α -

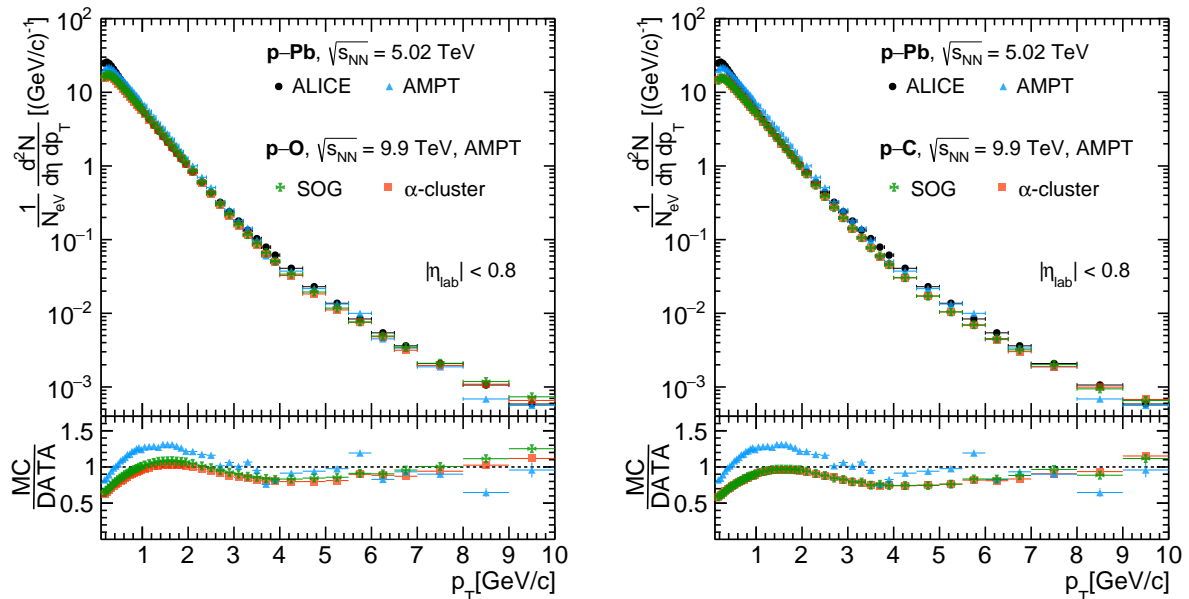


FIG. 9. (Color online) Upper panel shows comparison of transverse momentum spectra measured at ALICE [90] for minimum bias p-Pb collisions at $\sqrt{s_{\text{NN}}} = 5.02$ TeV with the predictions from AMPT with $\sigma_{\text{gg}} = 3$ mb for p-Pb collisions at $\sqrt{s_{\text{NN}}} = 5.02$ TeV as well as p-O (left) and p-C (right) collisions at $\sqrt{s_{\text{NN}}} = 9.9$ TeV. The lower panel shows the ratio of p_T -spectra of p-Pb, p-O and p-C collisions in AMPT to ALICE measurements for p-Pb collisions.

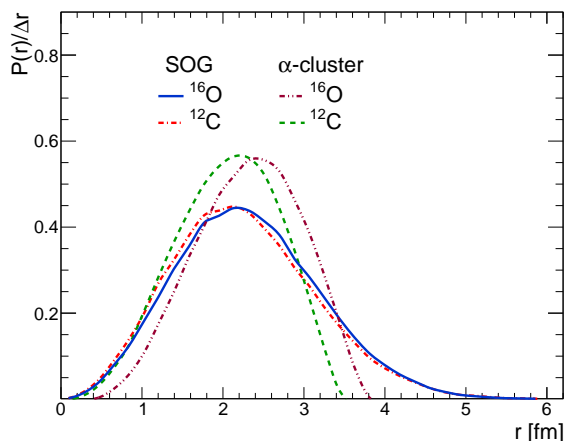


FIG. 10. (Color Online) Probability distribution of the radial position of the nucleons inside ^{12}C and ^{16}O nucleus considering SOG and α -cluster nuclear density profiles.

cluster nuclear distribution is compared with the SOG nuclear distribution for both ^{12}C and ^{16}O nuclei where the α -cluster nuclear distribution retains a more compact structure as compared to the SOG nuclear density profile. In addition, one finds that the peak positions of the probability distribution for both the nuclear density profiles are slightly lowered for the ^{12}C case when compared with the ^{16}O nucleus.

-
- [1] J. Adam *et al.* [ALICE Collaboration], Nature Phys. **13**, 535 (2017).
 [2] B. B. Abelev *et al.* [ALICE Collaboration], Phys. Lett. B **726**, 164 (2013).
 [3] V. Khachatryan *et al.* [CMS Collaboration], Phys. Rev. Lett. **116**, 172302 (2016).
 [4] B. B. Abelev *et al.* [ALICE Collaboration], Phys. Lett. B **728**, 25 (2014).
 [5] J. Adam *et al.* [ALICE Collaboration], Phys. Lett. B **760**, 720 (2016).
 [6] V. Khachatryan *et al.* [CMS Collaboration], Phys. Lett. B **765**, 193 (2017).
 [7] J. Brewer, A. Mazeliauskas and W. van der Schee, [arXiv:2103.01939 [hep-ph]].
 [8] R. Katz, C. A. G. Prado, J. Noronha-Hostler and A. A. P. Suaide, Phys. Rev. C **102**, 041901 (2020).

- [9] U. Heinz and R. Snellings, *Ann. Rev. Nucl. Part. Sci.* **63**, 123 (2013).
- [10] J. Y. Ollitrault, *Phys. Rev. D* **46**, 229 (1992).
- [11] S. A. Voloshin, A. M. Poskanzer and R. Snellings, *Landolt-Bornstein* **23**, 293 (2010).
- [12] S. Voloshin and Y. Zhang, *Z. Phys. C* **70**, 665 (1996).
- [13] J. Adams *et al.* [STAR Collaboration], *Nucl. Phys. A* **757**, 102 (2005).
- [14] G. Giacalone, J. Jia and C. Zhang, *Phys. Rev. Lett.* **127**, 242301 (2021).
- [15] M. R. Haque, M. Nasim and B. Mohanty, *J. Phys. G* **46**, 085104 (2019).
- [16] D. Behera, S. Prasad, N. Mallick and R. Sahoo, *Phys. Rev. D* **108**, 054022 (2023).
- [17] S. Acharya *et al.* [ALICE Collaboration], *JHEP* **10**, 152 (2021).
- [18] S. Acharya *et al.* [ALICE Collaboration], *Phys. Lett. B* **784**, 82 (2018).
- [19] A. M. Sirunyan *et al.* [CMS Collaboration], *Phys. Rev. C* **100**, 044902 (2019).
- [20] G. Aad *et al.* [ATLAS Collaboration], *Phys. Rev. C* **101**, 024906 (2020).
- [21] C. Aidala *et al.* [PHENIX Collaboration], *Nature Phys.* **15**, 214 (2019).
- [22] S. Chatrchyan *et al.* [CMS Collaboration], *Phys. Lett. B* **718**, 795 (2013).
- [23] B. Abelev *et al.* [ALICE Collaboration], *Phys. Lett. B* **719**, 29 (2013).
- [24] G. Aad *et al.* [ATLAS Collaboration], *Phys. Rev. Lett.* **110**, 182302 (2013).
- [25] S. Chatrchyan *et al.* [CMS Collaboration], *Phys. Lett. B* **724**, 213 (2013).
- [26] S. Acharya *et al.* [ALICE Collaboration], *Phys. Rev. Lett.* **123**, 142301 (2019).
- [27] B. B. Abelev *et al.* [ALICE Collaboration], *Phys. Rev. C* **90**, 054901 (2014).
- [28] S. Y. Tang, L. Zheng, X. M. Zhang and R. Z. Wan, *Nucl. Sci. Tech.* **35**, 32 (2024).
- [29] G. Gamow, *Constitution of Atomic Nuclei and Radioactivity*, International series of monographs on physics PCMI collection, Clarendon Press (1931).
- [30] J. A. Wheeler, *Phys. Rev.* **52**, 1083 (1937).
- [31] R. Bijker and F. Iachello, *Phys. Rev. Lett.* **112**, 152501 (2014).
- [32] X. B. Wang, G. X. Dong, Z. C. Gao, Y. S. Chen and C. W. Shen, *Phys. Lett. B* **790**, 498 (2019).
- [33] W. B. He, Y. G. Ma, X. G. Cao, X. Z. Cai and G. Q. Zhang, *Phys. Rev. Lett.* **113**, 032506 (2014).
- [34] J. He, W. B. He, Y. G. Ma and S. Zhang, *Phys. Rev. C* **104**, 044902 (2021).
- [35] M. Rybczyński and W. Broniowski, *Phys. Rev. C* **100**, 064912 (2019).
- [36] M. D. Sievert and J. Noronha-Hostler, *Phys. Rev. C* **100**, 024904 (2019).
- [37] S. Huang, Z. Chen, J. Jia and W. Li, *Phys. Rev. C* **101**, 021901 (2020).
- [38] D. Behera, N. Mallick, S. Tripathy, S. Prasad, A. N. Mishra and R. Sahoo, *Eur. Phys. J. A* **58**, 175 (2022).
- [39] Y. A. Li, S. Zhang and Y. G. Ma, *Phys. Rev. C* **102**, 054907 (2020).
- [40] P. Bozek, W. Broniowski, E. Ruiz Arriola and M. Rybczyński, *Phys. Rev. C* **90**, 064902 (2014).
- [41] W. Broniowski and E. Ruiz Arriola, *Phys. Rev. Lett.* **112**, 112501 (2014).
- [42] S. H. Lim, J. Carlson, C. Loizides, D. Lonardoni, J. E. Lynn, J. L. Nagle, J. D. Orjuela Koop and J. Ouellette, *Phys. Rev. C* **99**, 044904 (2019).
- [43] N. Summerfield, B. N. Lu, C. Plumberg, D. Lee, J. Noronha-Hostler and A. Timmins, *Phys. Rev. C* **104**, L041901 (2021).
- [44] B. Schenke, C. Shen and P. Tribedy, *Phys. Rev. C* **102**, 044905 (2020).
- [45] A. Huss, A. Kurkela, A. Mazeliauskas, R. Paatelainen, W. van der Schee and U. A. Wiedemann, *Phys. Rev. C* **103**, 054903 (2021).
- [46] B. G. Zakharov, *JHEP* **09**, 087 (2021).
- [47] D. Behera, S. Deb, C. R. Singh and R. Sahoo, *Phys. Rev. C* **109**, 014902 (2024).
- [48] C. Ding, L. G. Pang, S. Zhang and Y. G. Ma, *Chin. Phys. C* **47**, 024105 (2023).
- [49] Y. Z. Wang, S. Zhang and Y. G. Ma, *Phys. Lett. B* **831**, 137198 (2022).
- [50] M. Rybczyński, M. Piotrowska and W. Broniowski, *Phys. Rev. C* **97**, 034912 (2018).
- [51] A. Svetlichnyi, S. Savenkov, R. Nepeivoda and I. Pshenichnov, *MDPI Physics* **5**, 381 (2023).
- [52] B. Zhang, C. M. Ko, B. A. Li and Z. w. Lin, *Phys. Rev. C* **61**, 067901 (2000).
- [53] Z. W. Lin, C. M. Ko, B. A. Li, B. Zhang and S. Pal, *Phys. Rev. C* **72**, 064901 (2005).
- [54] X. N. Wang and M. Gyulassy, *Phys. Rev. D* **44**, 3501 (1991).
- [55] B. Zhang, *Comput. Phys. Commun.* **109**, 193 (1998).
- [56] Y. He and Z. W. Lin, *Phys. Rev. C* **96**, 014910 (2017).
- [57] B. Andersson, G. Gustafson, G. Ingelman and T. Sjöstrand, *Phys. Rept.* **97**, 31 (1983).
- [58] Z. w. Lin and C. M. Ko, *Phys. Rev. C* **65**, 034904 (2002).
- [59] B. Li, A. T. Sustich, B. Zhang and C. M. Ko, *Int. J. Mod. Phys. E* **10**, 267 (2001).
- [60] B. A. Li and C. M. Ko, *Phys. Rev. C* **52**, 2037 (1995).
- [61] S. Prasad, N. Mallick, S. Tripathy and R. Sahoo, *Phys. Rev. D* **107**, 074011 (2023).
- [62] S. K. Das, *et al.* *Int. J. Mod. Phys. E* **31**, 12 (2022).
- [63] J. Altmann, *et al.* *Eur. Phys. J. C* **84**, 421 (2024).
- [64] N. Mallick, R. Sahoo, S. Tripathy and A. Ortiz, *J. Phys. G* **48**, 045104 (2021).
- [65] N. Mallick, S. Tripathy and R. Sahoo, *Eur. Phys. J. C* **82**, 524 (2022).
- [66] N. Mallick, S. Prasad, A. N. Mishra, R. Sahoo and G. G. Barnaföldi, *Phys. Rev. D* **107**, 094001 (2023).
- [67] N. Mallick, S. Prasad, A. N. Mishra, R. Sahoo and G. G. Barnaföldi, *Phys. Rev. D* **105**, 114022 (2022).
- [68] C. Loizides, J. Kamin and D. d’Enterria, *Phys. Rev. C* **97**, 054910 (2018). [erratum: *Phys. Rev. C* **99**, 019901 (2019)]
- [69] C. Loizides, *et. al.*, <https://tglaubermc.hepforge.org/>.
- [70] A. Shukla, S. Åberg and S. K. Patra, *J. Phys. G: Nucl. Part. Phys.* **38**, 095103 (2011).
- [71] H. de Vries, C. W. de Jager and C. de Vries, *At. Data Nucl. Data Tables* **36**, 495 (1987).
- [72] I. Angeli and K. P. Marinova, *Atom. Data Nucl. Data Tabl.* **99**, 69 (2013).
- [73] B. B. Abelev *et al.* [ALICE Collaboration], *JHEP* **06**, 190 (2015).
- [74] A. Bilandzic, R. Snellings and S. Voloshin, *Phys. Rev. C* **83**, 044913 (2011).

- [75] Y. Zhou, X. Zhu, P. Li and H. Song, Phys. Rev. C **91**, 064908 (2015).
- [76] Y. Zhou [ALICE Collaboration], Nucl. Phys. A **931**, 949 (2014).
- [77] M. Aaboud *et al.* [ATLAS Collaboration], Eur. Phys. J. C **77**, 428 (2017).
- [78] W. Li [CMS Collaboration], Nucl. Phys. A **932**, 373 (2014).
- [79] B. B. Abelev *et al.* [ALICE Collaboration], Eur. Phys. J. C **74**, 3054 (2014).
- [80] B. Abelev *et al.* [ALICE Collaboration], Phys. Rev. Lett. **110**, 082302 (2013).
- [81] P. Bozek, Phys. Rev. C **85**, 014911 (2012)
- [82] J. Q. Tao, H. B. He, H. Zheng, W. C. Zhang, X. Q. Liu, L. L. Zhu and A. Bonasera, Nucl. Sci. Tech. **34**, 172 (2023).
- [83] S. Acharya *et al.* [ALICE Collaboration], Phys. Lett. B **845**, 137730 (2023).
- [84] H. Petersen, G. Y. Qin, S. A. Bass and B. Muller, Phys. Rev. C **82**, 041901 (2010).
- [85] A. Bzdak, B. Schenke, P. Tribedy and R. Venugopalan, Phys. Rev. C **87**, 064906 (2013).
- [86] J. D. Orjuela Koop, A. Adare, D. McGlinchey and J. L. Nagle, Phys. Rev. C **92**, 054903 (2015).
- [87] C. Aidala *et al.* [PHENIX Collaboration], Phys. Rev. C **95**, 034910 (2017).
- [88] N. J. Abdulameer *et al.* [PHENIX Collaboration], Phys. Rev. C **107**, 024907 (2023).
- [89] U. A. Acharya *et al.* [PHENIX Collaboration], Phys. Rev. C **105**, 024901 (2022).
- [90] S. Acharya *et al.* [ALICE Collaboration], JHEP **11**, 013 (2018).